This is the accepted manuscript made available via CHORUS. The article has been published as:

Controlling interface structure in nanoglasses produced through hydrostatic compression of amorphous nanoparticles

Bin Cheng and Jason R. Trelewicz

Phys. Rev. Materials **3**, 035602 — Published 20 March 2019

DOI: 10.1103/PhysRevMaterials.3.035602

Interface Structure and Design in Nanoglasses Produced through Hydrostatic Compression of Amorphous Nanoparticles

Bin Cheng[1] and Jason R. Trelewicz[1,2,*]

[1]Department of Materials Science and Chemical Engineering, Stony Brook University, Stony Brook, NY 11794

[2]Institute for Advanced Computational Science, Stony Brook University, Stony Brook, NY 11794

*Corresponding Author at Stony Brook University: Jason.trelewicz@stonybrook.edu

Abstract

Controlling glass-glass interfaces in metallic nanoglasses is essential for tuning their mechanical properties and in particular, the ability to inhibit severe strain localization through distributed shear band formation. In this paper, molecular dynamics are employed to quantify the structural characteristics of interfaces in a scalable nanoglass model produced through hydrostatic compression of amorphous nanoparticles. Using a new framework for distinguishing interfaces from amorphous grains based on the correlation between dilatation and atomic volume distributions, we show that the interfaces in our nanoglass model exhibit a volume fraction of 0.36, width of approximately 2 nm, excess free volume of 1 – 2 %, and full icosahedral (FI) fraction roughly 30% that of a bulk metallic glass counterpart. While these characteristics are quantitatively unique relative to other nanoglass models (e.g. planar interfaces and Poisson-Voronoi constructions), they are consistent with experimental results reported for nanoglasses consolidated from glassy nanoparticles produced through inert gas condensation. Increasing the consolidation temperature enhanced the FI fraction with a strong bias to the interfaces, thus demonstrating a new route for tuning interfacial properties in nanoglasses.

Keywords: metallic glasses, interfaces, nanoglasses, nanoparticles, molecular dynamics

1. Introduction

Nanoglasses represent a new class of noncrystalline solids with microstructures that resemble a nanocrystalline state, i.e. nanoscale grains embedded within a high volume fraction of interfacial material denoted the grain boundary network. In contrast to nanocrystalline solids, the grains in nanoglasses are instead amorphous in nature and produce glass-glass interfaces defined by a combination of structural and chemical heterogeneities [1,2]. These unique microstructures have been linked to a range of unique properties relative to monolithic bulk metallic glasses (BMGs) including improved mechanical performance [3,4], enhanced ferromagnetism [5,6], and unusually high thermal stability [7,8]. Experimental nanoglasses were first reported by Jing et al. [9] where inert gas condensation was used to synthesize nanometer-sized glassy clusters from a Pd-Fe-Si alloy, which were subsequently consolidated to produce a nanoglass at pressures up to 5 GPa. Recently, nanoglasses have been synthesized through other processing techniques such as magnetron sputtering [10,11], electrodeposition [12], and severe plastic deformation [13,14]. Due in large part to this resurgence in the production of nanoglasses, there is a growing interest in understanding the nature of glass-glass interfaces and their implications for tuning material physics at the nanoscale [15].

Structural characterization has focused on capturing the physical presence of glass-glass interfaces, which generally exhibit a reduced density relative to the amorphous grains [2]. Positron annihilation spectroscopy and small angle X-ray scattering on $Sc_{75}Fe_{25}$ nanoglasses synthesized via inert gas condensation showed that interfacial regions were present in volume fractions of 31 to 44% with widths of 0.8 to 1.2 nm; both attributes were demonstrated to be tailorable through annealing [8]. Interfaces were also observed in magnetron sputter deposited Au-based nanoglasses through bright-field transmission electron microscopy and exhibited

widths of 2 to 3 nm with amorphous grain sizes ranging from 20 to 30 nm [11]. Complementary atomistic models have been leveraged in concert with experiments to probe atomic-level features of glass-glass interfaces. Bicrystal-like nanoglass models were generated by Ritter et al. [16] by joining two planar relaxed glass-glass surfaces produced from a $Cu_{64}Zr_{36}$ alloy. The resulting interfacial region was approximately 1 nm thick and characterized by an enhanced potential energy, excess free volume of 1 to 2%, and defective short-range order. A core-shell structure was constructed by Adjaoud et al. [17] to quantify surface segregation in Cu-Zr nanoglasses. Core enrichment of Zr was found to be coupled with surface depletion and attributed to the larger cohesive energy of Zr promoting preferential occupation of atomic sites that optimize the binding energy of the system.

The connection between interfacial defect state, nanoglass length scales, and mechanical behavior has also been explored widely through atomistic simulations using three-dimensional models that have included both columnar and equiaxed-like amorphous grain structures. The columnar nanoglass model developed by Soqu et al. [18] contained columnar hexagonal grains produced through the consolidation of glassy nanopillars extracted from a simulated quenched BMG sample. Adibi et al. [19] instead applied a Poisson-Voronoi tessellation to a quenched BMG nanopillar where random atomic position shifts were performed within each Voronoi cell to effectively create glass-glass interfaces; other models including nanoglasses containing bimodal grain size distributions have also employed Poission-Voronoi constructions [20]. Under uniaxial tensile loading of the columnar and Voronoi type structures, severe shear localization was suppressed through the introduction of glass-glass interfaces containing defective short-range order and excess free volume. Plastic shear strain was also shown to be preferentially accommodated within the interfacial regions, which in turn promoted the formation of multiple

shear bands [18] rather than a primary shear front common in BMG models where plastic strain subsequently localizes.

While the columnar and Voronoi nanoglass models have provided valuable insights into the nature of glass-glass interfaces and their implications for the process of shear localization, they are generally limited by their idealized configurations and in the case of the columnar model, scalability especially with respect to network effects on interfacial plasticity. In this paper, we expand on the core-shell and columnar nanoglass frameworks to produce a scalable nanoglass model through hydrostatic compression of amorphous nanoparticles stacked in close-packed configurations. A new computational method based on the correlation between dilatation and atomic volume distributions during consolidation is also developed to distinguish atoms composing the glass-glass interfacial regions from those located within the amorphous grains. With interfaces precisely indexed, their structural characteristics including volume fraction, width, excess free volume, and short-range order are quantified and shown to be consistent with experimental results reported for nanoglasses produced through inert gas condensation techniques. Interfacial structure is finally manipulated by varying the consolidation temperature, thus demonstrating a new route for tuning the interfacial properties in simulated nanoglass structures.

2. Simulation Methods

Molecular dynamic (MD) simulations were performed using the LAMMPS package [21] with atomic interactions in the Cu-Zr system described by the embedded-atom method (EAM) potential developed by Mendelev et al. [22] To build the nanoglass models, a $Cu_{64}Zr_{36}$ amorphous alloy was first generated by slowly quenching a Cu-Zr mixture equilibrated at 2000 K for 2 ns to 50 K using a cooling rate of 0.01 $K \cdot ps^{-1}$. Spherical amorphous nanoparticles with a

diameter of 15 nm were extracted from the $Cu_{64}Zr_{36}$ amorphous sample and used to generate the initial structure for consolidation. A total of 64 nanoparticles containing approximately 7 million atoms were stacked in a close-packed face-centered cubic (FCC) configuration and prior to consolidation, subjected to an energy minimization procedure to eliminate atom overlap with a final relative energy convergence of 10^{-12}.

Energy minimized structures were consolidated over the course of 100 ps at a temperature of 50 K under hydrostatic pressure varied over the range of 1.5 – 9 GPa. The isobaric-isothermal (NPT) ensemble was employed to control pressure and temperature during the consolidation simulations with a constant integration time step of 2 fs; all subsequent analysis of these structures was conducted in the unloaded state with pressure-free conditions achieved in all dimensions. The role of temperature in densification was explored using the same procedures as described above with the exception that a smaller nanoparticle diameter of 10 nm was used to reduce the total system size (using the same number of nanoparticles) to approximately 2 million atoms, which in turn reduced the computational resources required for each simulation. These structures were heated to four different consolidation temperatures of 50, 300, 500, and 800 K using a ramp rate of 1 $K \cdot ps^{-1}$. Hydrostatic pressure was then applied at temperature for 100 ps with a magnitude that varied based on the minimum pressure required to achieve full density at the different consolidation temperatures. Each structure was finally unloaded and cooled down to 50 K at a rate of 1 $K \cdot ps^{-1}$ for characterization. We note that the highest temperature employed in our simulations exceeded both the glass transition and crystallization temperatures of the selected Cu-Zr amorphous alloy (i.e., 737 and 776 K, respectively [23]). However, the extremely short simulation times accessible via MD preclude crystallization at 800 K, thereby

allowing us to enhance the kinetics during consolidation by exceeding the crystallization temperature of the alloy.

Interfacial regions in the consolidated nanoglasses were identified using atomic volume distributions coupled with the volumetric strain, which represents the first invariant of the strain tensor using the unconsolidated structure as a reference state. The atomic volume was determined using the Voronoi tessellation method described in Ritter et al. [16] where Voronoi polyhedra were constructed around each atom with planar faces perpendicular to the lines joining the atom to its nearest neighbors. The Voronoi index was also catalogued for each atom's polyhedron and used to identify Cu-centered full icosahedra, which represent the most common short-range order in the Cu-Zr metallic glass system [24,25]. Finally, a surface mesh method [26] was adopted to quantify the void volume fraction as a function of consolidation pressure, time, and pressure ramp rate. The open-source OVTIO software [27] was used for visualization of the nanoglass structures at various stages of consolidation, and custom codes were developed for fitting the volumetric strain-indexed atomic volume distributions. A cutoff radius of 3.5 Å was employed in the volumetric strain and surface mesh calculations, both of which required specification of a nearest neighbor distance. Local temperature during consolidation was also calculated using the same cutoff radius and corresponded to an average value from a volume of 180 $Å^3$.

3. Nanoglass Consolidation and Effect of Hydrostatic Loading Parameters

Consolidation of the amorphous nanoparticles was accomplished using hydrostatic loading at a temperature of 50 K, which was selected to minimize structural evolution driven by thermal energy and in turn, isolate the role of mechanical forces in interface formation at matting

particle surfaces under hydrostatic stresses. The initial FCC stacking configuration of the amorphous nanoparticles is shown in Fig. 1(a) where Cu and Zr atoms are colored red and blue, respectively. The application of periodic boundary conditions on all faces of the initial nanoparticle configuration ensures bulk continuity was retained throughout the consolidation process. For a structure containing spheres of equal diameter, the FCC stacking sequence maximizes the packing density and thus accelerates elimination of the voids initially present between nanoparticles. We note that due to the large numbers of atoms in the structure (~7 million atoms), the individual particles are difficult to distinguish; however, the point of Fig. 1(a) is to illustrate the initial stacking configuration relative to the consolidated structure in Fig. 2(a). In this section, we explore the role of pressure, time, and pressure ramp rate on structural consolidation with specific focus on void elimination and thermal spike formation, which collectively represent critical parameters for achieving fully dense nanoglass models containing interfacial regions of varying free volume.

The volumetric strain profile for the stacked nanoparticle structure is shown in Fig. 1(b) and as expected, the nanoparticles exhibited a null dilatation prior to the application of a hydrostatic compressive load. The atomic distribution for this configuration following energy minimization is shown in Fig. 1(c) relative to the BMG model used for initial generation of the nanoparticles. The first peak at approximately 12.5 $Å^3$ captures the atomic volume distribution for the Cu atoms while the second peak at approximately 22.5 $Å^3$ is for Zr. Despite the appearance of minor serrations that were attributed to the nanoparticle configuration only being subjected to a conjugant gradient energy minimization and not a subsequent thermal relaxation process, the atomic volume distribution for the unconsolidated nanoparticles was consistent with the BMG. However, we note a subtle albeit important anomaly in this distribution where an

increased fraction of atoms with larger atomic volumes (i.e. > 15 and 25 $Å^3$ for the Cu and Zr peaks, respectively) were apparent as shown in the inset of Fig. 1(c). This increase was attributed to the atoms located at the surface of the nanoparticles exhibiting larger Voronoi volumes relative to atoms within the bulk due to the free surface condition facilitating localized atomic dilatation.

The consolidated nanoglass structure generated by application of a 9 GPa hydrostatic pressure for 100 ps is shown in Fig. 2(a) and appeared structurally homogenous and free of surface voids. Regions of high volumetric strain are shown in the slice through the y-z plane depicted in Fig. 2(b), and through comparison with the unconsolidated structure in Fig. 1(b), encompassed atoms in close proximity to the nanoparticle surfaces prior to densification. Material flow during consolidation was thus concentrated to surface layers while the central regions of the nanoparticles were free of deformation via shear band formation. The atomic volume distribution of the consolidated nanoglass is shown in Fig. 2(c) relative to the BMG. While densification eliminated surface atoms with larger Voronoi volumes as substantiated by the elimination of atomic volumes greater than 15 and 25 $Å^3$ for the Cu and Zr peaks, respectively, the entire distribution for the consolidated nanoglass shifted to larger atomic volumes. This is evidenced by the reduction in both the Cu and Zr peak intensities, which was coupled with a shift in the peak shoulders to larger atomic volumes as shown for the copper peak in inset of Fig. 2(c). Compared with the BMG, the atomic volume distribution evolved to contain a greater fraction of atoms with larger average Voronoi volumes for both atom types, thus suggesting regions of excess free volume were present in the consolidated nanoglass, which is the focus of the following section.

Consolidation pressure played a critical role in densification of the nanoglass samples as captured by the inverse scaling of void volume fraction with pressure in Fig. 3(a). A void-free nanoglass model was only achieved at a pressure of 9 GPa, which is more than double the pressure commonly required in experiments[8] and attributed to the high pressure ramp rates inherent to the MD technique combined with the low consolidation temperature. The void volume fraction also scaled inversely with the pressure ramp rate as shown in Fig. 3(b), eventually converging to a fully dense structure with instantaneous application of the consolidation pressure (i.e., denoted on the plot as instantaneous pressure ramp or IPR). However, such an extreme pressure ramp generated large thermal spikes, which were concentrated to atoms in the surface layers of the nanoparticles that contribute to volumetric strain accumulation during consolidation as illustrated in Fig. 3(c). The sharp peak in temperature following instantaneous application of pressure was attributed to the rapid release of stored elastic energy during shock loading. While reducing the pressure ramp rate allayed the severity of this initial temperature spike, a second peak emerged in the temperature trends that instead derived from the thermal energy released due to material flow during consolidation.

Collective optimization of the consolidation temperature, pressure, pressure ramp rate, and time must consider the formation of these local thermal spikes and their implications for the resulting nanoglass structure. In particular, a localized temperature excursion can promote large thermal gradients that in turn, will inevitably produce non-uniform structural relaxation during consolidation. This effect will be most profound for atoms primarily contributing to densification (i.e. in the surface layers of the amorphous nanoparticles as noted above), which experienced the largest local temperature increase in the inset of Fig. 3(c). A reduction in the pressure ramp rate allayed the severity of these thermal spikes, but it was also accompanied by

enhanced void retention from Fig. 3(b). We therefore can identify an optimal set of consolidation conditions that minimize thermal spikes while producing a void-free nanoglass structure. A pressure ramp rate of 1.5 GPa·ps^{-1} was adequate for producing a void-free nanoglass from Fig. 3(b) while alleviating the severe thermal spike associated with instantaneous application of a hydrostatic load in Fig. 3(c). Employing this pressure ramp rate and a total consolidation time of 100 ps, a consolidation pressure of 9 GPa eliminated the formation of voids in Fig. 3(a) for the sample produced from 15 nm diameter nanoparticles. This set of conditions was thus used in the generation of a void-free nanoglass model with minimal structural evolution from localized thermal gradients.

4. Distinguishing Interfaces from Amorphous Grains in Consolidated Nanoglasses

Hydrostatic compression of the nanoparticle configurations generated a fully dense amorphous structure containing regions of high volumetric strain and larger average Voronoi volumes relative to the initial nanoparticles. While it is reasonable to assume the regions of high volumetric strain are largely responsible for the shift in Voronoi volumes due to the accumulation of excess free volume at the matting nanoparticle surfaces during consolidation, a criterion is needed to distinguish these regions of excess free volume from the bulk glass structure. Based on the postulated correlation between dilatation and atomic volume, a method was devised to identify atoms composing the glass-glass interface by sorting each atom's atomic volume as a function of volumetric strain. In this approach, we define the atomic volume variance, χ^2, between the fraction of atoms in the consolidated state, $F_C(k)$, and a predefined reference state, $F_R(k)$ as:

$$\chi^2 = \sum_{k=1}^{N}[F_C(k) - F_R(k)]^2 \quad (1)$$

where k stands for the k^{th} bin of the cumulative atomic volume distribution discretized accordinging to each atom's value of volumetric strain, ε_v. N is the total number of bins employed in the distribution function, and the $Cu_{64}Zr_{36}$ BMG was used as the reference state. We note this choice of reference state neglects the anomalous atomic volume of the surface atoms in the unconsolidated nanoparticles. However, because our objective is to distinguish interfacial regions composed of excess free volume from the bulk of the consolidated glass with an atomic volume distribution unaffected by free surface effects, the BMG sample is an appropriate reference state.

The cumulative atomic volume distribution for the consolidated nanoglass was discretized using a volumetric strain cutoff, ε_v^{cutoff}, varied over the range of 0 – 0.5 in strain increments of 0.001. Atomic volume distributions were then generated for atoms with volumetric strain values of $0 - \varepsilon_v^{cutoff}$ and used to calculate χ^2 as a function of ε_v^{cutoff}. Three such distributions are shown for the Cu atoms in the consolidated structure in Fig. 4(a-c) relative to the BMG for ε_v^{cutoff} values of 0.01, 0.1, and 0.2, respectively. Atoms with $\varepsilon_v \leq \varepsilon_v^{cutoff}$ are colored green in the insets of these plots and for the case where $\varepsilon_v \leq 0.01$ in Fig. 4(a), the highlighted atoms were concentrated in the central region of the consolidated nanoparticles. This subset of atoms exhibited a shift in the distribution to lower atomic volumes relative to the BMG, indicating they did indeed sustain a volumetric compression during consolidation and consistent with the core-shell model proposed by Danilov et al. [28] for consolidated gas-condensed glassy spheres. Increasing ε_v^{cutoff} to 0.1 captured a greater fraction of atoms within the consolidated nanoparticles as shown in the inset of Fig. 4(b). The atomic volume distribution for this subset of atoms more closely resembled the BMG due to the addition of atoms in the outer shell of the consolidated sphere with Voronoi volumes marginally greater than the mean value for Cu. A further increase

in ε_v^{cutoff} to 0.2 incorporated atoms in the regions beyond the outer shells of the consolidated nanoparticles shown in the inset of Fig. 4(c). The corresponding shift in the distribution to larger atomic volumes relative to the BMG indicated that atoms experiencing larger volumetric strains during consolidation exhibited larger Voronoi volumes, which were concentrated within the surface layers primarily contributing to densification.

The value of χ^2 determined via Eq. (1) for each of the distributions is summarized in the plots of Fig. 4 for each ε_v range defined by the value of ε_v^{cutoff}. As ε_v^{cutoff} was increased from 0.01 to 0.1, χ^2 decreased from 2.92 x 10^{-5} to 4.82 x 10^{-6} and consistent with the atomic volume distribution for the selected atoms in the consolidated structure converging toward the distribution for the BMG. A further increase in ε_v^{cutoff} to 0.2 was accompanied by a subtle increase in the variance to 8.04 x 10^{-6}, thus signifying the presence of an inflection at a distinct value of ε_v^{cutoff}. To identify the inflection point, χ^2 is plotted as a function of ε_v^{cutoff} in Fig. 5(a), from which a minimum is identified at $\varepsilon_v^{cutoff} = 0.088$. Denoted the threshold volumetric strain, $\varepsilon_v^{threshold}$, the atomic volume distribution for atoms in the consolidated structure with $\varepsilon_v \leq 0.088$ most closely matched the atomic volume distribution of the BMG. Thus, the criterion $\varepsilon_v^{threshold} = 0.088$ was established to distinguish amorphous grains from the interfacial regions in the consolidated nanoglass.

From the insets of Fig. 5(a), the amorphous grains encompassed the core regions of the nanoparticles used to build the nanoglass for the structure with $\varepsilon_v^{threshold} = 0.088$ and its atomic volume distribution was nearly identical to the BMG in the lower panel of Fig. 5(b). Subtle discrepancies in the two distributions were attributed to the aforementioned effects related to the surfaces of the nanoparticles during consolidation including core compression and core-shell

relaxation. Conversely, the atomic volume distribution for the atoms within the interfacial regions between the amorphous grains in the upper panel of Fig. 5(b) significantly deviated from the BMG. Not only did the peaks for both Cu and Zr shift to larger atomic volumes, the overall distribution for each atom type was also skewed in the same direction and indicative of local dilatation in the regions between the core regions of the amorphous spheres. Interfaces in the consolidated nanoglasses are thus characterized by excess free volume relative to the cores of the amorphous nanoparticles, which was quantitatively distinguished using atomic volume distributions indexed based on the volumetric strain resulting from consolidation under hydrostatic compression.

5. Interface Structure and Design

To build a statistical representation of the interfacial structure in the subject nanoglasses, five distinct nanoglass models were consolidated using the 15 nm diameter amorphous nanoparticles and characterized using the volumetric strain assorted atomic volume distribution fitting method. The results are tabulated in Table 1 and include the average values for the BMG and nanoglass with the latter also delineated for the interfaces and amorphous grains. The interfacial volume fraction was calculated by normalizing the sum of the atomic volumes for atoms with a volumetric strain greater than $\varepsilon_v^{threshold}$ by the total volume of the nanoglass. Using a $\varepsilon_v^{threshold} = 0.088$, which represents the average value determined from all five of the nanoglass models, the interfacial volume fraction was determined to be 0.36. This value is consistent with the experimental value of 0.35 obtained from $Sc_{75}Fe_{25}$ nanoglasses consolidated from nanoparticles produced by inert gas condensation [8].

The nanoglass atomic volume distributions were compared with the distribution for the BMG and deviations quantified using the variance as shown in Table 1. When delineated for the interfaces and amorphous grains, differences in the variance evidently derived from the interfaces, which exhibited a variance relative to the BMG of more than 20 times greater than the interior of the amorphous grains. The variance in the atomic volume distribution was correlated to the local average atomic volumes for both atom types. As summarized in Table 1, the average atomic volume of the Cu and Zr atoms in the interfacial region were greater than their counterparts within the amorphous grains, which were in good agreement with the average atomic volumes ascertained from the BMG model. This dilatation of approximately 1.3% can thus be viewed as the excess free volume of the interfaces with respect to the amorphous grains and is consistent with the planar glass-glass interfaces studied by Ritter et al. [16] in a nominally identical $Cu_{64}Zr_{36}$ amorphous alloy. Combined with the partitioning of volumetric strain to the interfaces (evident in Table 1 by the order of magnitude difference between the interfaces and amorphous grains), these results confirm our fundamental assumption that interfacial regions of excess free volume form due to heterogeneous volumetric strain accumulation during consolidation.

The FI fraction was used to quantify short-range order and from Table 1, was nearly 50% less in the interfaces relative to the amorphous grains and consistent with the excess free volume present in the interfacial regions. Interestingly, the FI fraction within the amorphous grains was also less than the BMG, indicating that the consolidation process reduced the prevalence of short-range ordering in the central regions of the amorphous nanoparticles. The reduction in the number of Cu-centered full icosahedra was attributed to the depletion of Cu within the central regions of amorphous grains as evident in Table 1. This effect derives from segregation of Cu to

the surfaces of the nanoparticles demonstrated by Adjaoud and Albe [17] with corresponding depletion within the cores, which was retained through consolidation in our simulations. Compared with the planar glass-glass interface model [16], the interfaces generated through amorphous nanoparticle consolidation exhibited a higher degree of disorder, which aligns with the consolidation process impacting the FI fraction in the amorphous grains relative to the BMG. In fact, the interfacial FI fraction in the nanoglasses was in good agreement with values reported for shear bands [29] and consistent with the use of mechanical loading for consolidation. We finally note that subtle segregation of Cu to the interfaces was observed whereas the amorphous grains were marginally enriched in Zr. This was attributed to Zr exhibiting a larger cohesive energy, which promotes preferential occupation of atomic sites that optimize the binding energy (i.e. central regions of the nanoparticles) while simultaneously reducing the surface energy as reported by Adjaoud et al. [17]

The volumetric strain, normalized atomic volume, and FI fraction were mapped along two directions as shown in the 5 nm slice extracted from the y-z plane in Fig. 6(a); the close-packed plane is also depicted for reference. The volumetric strain legend was scaled specifically from the $\varepsilon_v^{threshold}$ to highlight the interfacial atoms relative to the amorphous grains, which appear black in this indexing scheme. Two distinctive features can be identified in the consolidated structure: interfaces separating the amorphous grains that derived from the matting surfaces of two nanoparticles and triple junctions that formed from the free space between four matting nanoparticles. From the 5nm-thick slice extracted from the y-z plane, the width of the interfacial region can be seen to vary considerably between the interfaces and triple junctions. Quantitative mapping of the interfacial properties along the direction oriented 45° to the z-axis denoted by the red dashed line (i.e. through the interfaces separating the amorphous grains) is

summarized in Fig. 6(b). Periodicity in the average volumetric strain aligned with the characteristic length scale of the nanoglass defined nominally by the initial nanoparticle diameter (approximately 15 nm) and was also correlated with the regions of low FI fraction. Only subtle peaks could be identified in the normalized atomic volume that corresponded to the maxima in the volumetric strain, which produced an excess free volume of 1 – 2% in the interfaces. Based on the volumetric strain exceeding the threshold value, the interfacial width was calculated using 20 interfaces from the 5 different samples and determined to be 2.01 ± 0.23 nm.

The same structural attributes were mapped in Fig. 6(c) for the slice extracted through the triple junctions denoted by the blue dashed line and revealed comparable periodicity in the volumetric strain, which again correlated with the FI fraction; however, the difference in the normalized atomic volume in the triple junctions relative to the amorphous grains was far more pronounced, indicating excess free volume accumulation was biased to the triple junctions. Averaging over a total of 10 measurements from the 5 different samples, the width and excess free volume of the triple junctions was 8.54 ± 0.22 nm and approximately 6%, respectively, and thus more than four times the values determined for the interfaces. The reduced FI fractions in both the interfaces and triple junctions relative to the amorphous grains, which fell below 0.1 and roughly 30% of the average value for the BMG, were consistent with the excess free volume peaks. The FI fraction in the amorphous grains instead oscillated around the average value for the BMG, indicating these regions preserved the degree of order found in the glassy state used to produce the nanoparticles. Collectively, the interfaces and triple junctions contributed to the total interfacial volume fraction, which was determined to be 0.36 as previously noted. While this differs from both bicrystal-like [16] and Voronoi partitioned models [19,30,31], it is

consistent with powder-consolidated nanoglasses [8] and thus provides a better representation of experimental materials.

Manipulation of the interface structural state was accomplished by varying the consolidation temperature for a nanoglass sample produced from 10 nm diameter $Cu_{64}Zr_{36}$ amorphous nanoparticles. As noted in the methods section, the smaller nanoparticle size was deliberately selected to increase the efficiency of the simulations, but also serves to illuminate any potential grain size effects using an identical consolidation temperature of 50 K for one of the simulations. The void volume fraction is shown as a function of consolidation pressure in Fig. 7(a) for the two grain size nanoglasses consolidated at 50 K; results for the 10 nm grain size samples consolidated at the three higher temperatures are also included in this figure. A reduction in the initial nanoparticle size had little impact on the densification rate as evidenced by the similar consolidation curves at 50 K. Conversely, an increase the consolidation temperature considerably reduced the pressure required to achieve a fully dense structure. To isolate the effect of consolidation temperature, interfaces were analyzed for each structure at the minimum pressure required to achieve full density at the different temperatures.

The FI fraction and excess free volume are shown in Fig. 7(b) and 7(c), respectively, where the excess free volume, ν, was calculated from the difference in the average atomic volume, Ω_o, between the interfacial regions and amorphous grains also depicted in Fig. 7(c). The reduction in the initial nanoparticle size had no discernible impact on the FI fraction or excess free volume, indicating a change in the grain size from approximately 15 to 10 nm does not influence the interfacial characteristics of the nanoglass. Increasing the consolidation temperature instead produced a monotonic increase in the FI fraction in both the grain and interfacial regions that was accompanied by a decrease in the excess free volume and consistent

with relaxation processes in disordered solids [18,32]. However, the change in the FI fraction was far more pronounced in the interfaces, which exhibited a 42% increase relative to only a 13% increase in the grains. The reduction in excess free volume also derived primarily from a decrease in the average atomic volume of the atoms composing in the interfaces while the average atomic volume in the grains was independent of the consolidation temperature in Fig. 7(c). Biasing of these relaxation processes to the interfacial regions indicates that the consolidation temperature can be used to preferentially tailor the structural state of interfaces during processing and in turn, tune the properties and performance of nanoglasses produced through hydrostatic compression of amorphous nanoparticles.

6. Conclusions

MD simulations were used to construct a scalable nanoglass model by hydrostatically compressing amorphous $Cu_{64}Zr_{36}$ nanoparticles with two diameters of 10 and 15 nm for quantitatively characterizing the structural attributes of glass-glass interfaces. A new method was established for distinguishing interfaces from amorphous grains based on the correlation between dilatation and atomic volume distributions. Interfaces in the consolidated nanoglass models generally exhibited volume fractions, excess free volumes, and FI fractions that were consistent with experimental results reported for nanoglasses consolidated from glassy nanoparticles produced through inert gas condensation. Biased recovery of the FI fraction and excess free volume to the interfacial regions with increasing consolidation temperature (while remaining below the glass transition temperature) was indicative of interfacial relaxation, and provides new opportunities for tailoring the interfacial properties in metallic nanoglasses.

Acknowledgements

Support for this work was provided through the National Science Foundation under Award 1554411. The authors would like to thank Stony Brook Research Computing and Cyberinfrastructure and the Institute for Advanced Computational Science at Stony Brook University for access to the high-performance SeaWulf computing system, which was made possible by National Science Foundation Award 1531492. The authors also gratefully acknowledge the use of computing resources at the Center for Functional Nanomaterials, which is a US DOE Office of Science Facility at Brookhaven National Laboratory under Contract No. DE-SC0012704.

References

[1] H. Gleiter, T. Schimmel, and H. Hahn, Nano Today **9**, 17 (2014).
[2] H. Gleiter, Beilstein Journal of Nanotechnology **4**, 517 (2013).
[3] X. Wang, F. Jiang, H. Hahn, J. Li, H. Gleiter, J. Sun, and J. Fang, Scripta Materialia **116**, 95 (2016).
[4] X. L. Wang, F. Jiang, H. Hahn, J. Li, H. Gleiter, J. Sun, and J. X. Fang, Scripta Materialia **98**, 40 (2015).
[5] R. Witte *et al.*, Applied Physics Letters **103**, 073106 (2013).
[6] N. Chen, D. Wang, T. Feng, R. Kruk, K.-F. Yao, D. V. Louzguine-Luzgin, H. Hahn, and H. Gleiter, Nanoscale **7**, 6607 (2015).
[7] J. Q. Wang, N. Chen, P. Liu, Z. Wang, D. V. Louzguine-Luzgin, M. W. Chen, and J. H. Perepezko, Acta Mater. **79**, 30 (2014).
[8] J. X. Fang *et al.*, Nano Letters **12**, 458 (2012).
[9] J. Jing, A. Krämer, R. Birringer, H. Gleiter, and U. Gonser, Journal of Non-Crystalline Solids **113**, 167 (1989).
[10] N. Chen *et al.*, Acta Materialia **59**, 6433 (2011).
[11] N. Chen, D. V. Louzguine-Luzgin, G. Q. Xie, P. Sharma, J. H. Perepezko, M. Esashi, A. R. Yavari, and A. Inoue, Nanotechnology **24**, 045610 (2013).
[12] C. Guo, Y. Fang, B. Wu, S. Lan, G. Peng, X.-l. Wang, H. Hahn, H. Gleiter, and T. Feng, Materials Research Letters, 1 (2016).
[13] Q. P. Cao *et al.*, Acta Mater. **58**, 1276 (2010).
[14] H. Shao, Y. Xu, B. Shi, C. Yu, H. Hahn, H. Gleiter, and J. Li, Journal of Alloys and Compounds **548**, 77 (2013).
[15] Y. Liu, J. Liu, S. Sohn, Y. Li, J. J. Cha, and J. Schroers, Nature Communications **6**, 7043 (2015).
[16] Y. Ritter, D. Sopu, H. Gleiter, and K. Albe, Acta Materialia **59**, 6588 (2011).

[17] O. Adjaoud and K. Albe, Acta Materialia **113**, 284 (2016).
[18] D. Sopu, Y. Ritter, H. Gleiter, and K. Albe, Physical Review B **83**, 100202 (2011).
[19] S. Adibi, P. S. Branicio, Y.-W. Zhang, and S. P. Joshi, J. Appl. Phys. **116**, 043522 (2014).
[20] Z. D. Sha, P. S. Branicio, Q. X. Pei, Z. S. Liu, H. P. Lee, T. E. Tay, and T. J. Wang, Nanoscale **7**, 17404 (2015).
[21] S. Plimpton, Journal of Computational Physics **117**, 1 (1995).
[22] M. I. Mendelev, D. J. Sordelet, and M. J. Kramer, J. Appl. Phys. **102** (2007).
[23] N. Mattern, A. Schöps, U. Kühn, J. Acker, O. Khvostikova, and J. Eckert, Journal of Non-Crystalline Solids **354**, 1054 (2008).
[24] Y. Q. Cheng, H. W. Sheng, and E. Ma, Physical Review B **78**, 014207 (2008).
[25] Y. Q. Cheng, A. J. Cao, H. W. Sheng, and E. Ma, Acta Mater. **56**, 5263 (2008).
[26] A. Stukowski, Jom **66**, 399 (2014).
[27] A. Stukowski, Model Simul Mater Sc **18** (2010).
[28] D. Danilov, H. Hahn, H. Gleiter, and W. Wenzel, ACS Nano **10**, 3241 (2016).
[29] A. J. Cao, Y. Q. Cheng, and E. Ma, Acta Mater. **57**, 5146 (2009).
[30] S. Adibi, P. S. Branicio, and S. P. Joshi, Scientific Reports **5**, 15611 (2015).
[31] S. Adibi, Z.-D. Sha, P. S. Branicio, S. P. Joshi, Z.-S. Liu, and Y.-W. Zhang, Applied Physics Letters **103**, 211905 (2013).
[32] E. D. Cubuk *et al.*, Science **358**, 1033 (2017).

Tables

Table 1. Structural characteristics of the $Cu_{64}Zr_{36}$ bulk metallic glass (BMG) and nanoglass (NG) model consolidated using 15 nm diameter nanoparticles. The properties of the NG are further delineated for the amorphous grains and interfacial regions.

	BMG	NG	Grains	Interfaces
Volumetric Strain Threshold	-	0.088	-	-
Volume Fraction	-	-	0.64	0.36
Variance	-	1.52E-5	4.70E-6	9.57E-5
Average Volumetric Strain	-	0.11	0.023	0.25
Cu Atomic Volume ($Å^3$)	12.62	12.67	12.61	12.78
Zr Atomic Volume ($Å^3$)	22.31	22.35	22.26	22.52
FI Fraction	0.27	0.19	0.23	0.12
Cu Atom Fraction	0.64	0.64	0.63	0.65
Zr Atom Fraction	0.36	0.36	0.37	0.35

Figures

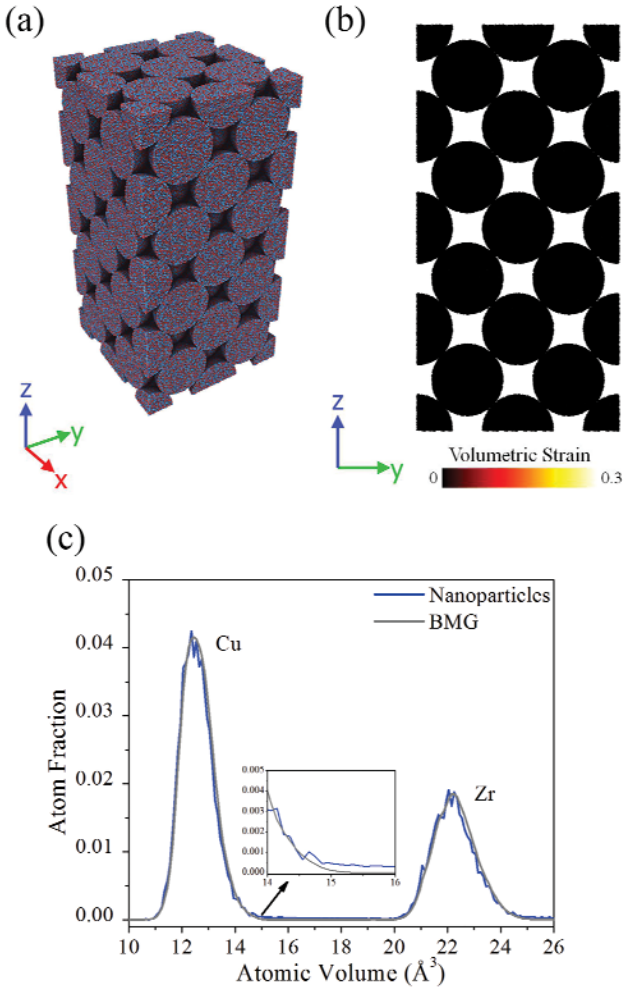

Fig. 1 (a) Initial FCC stacking configuration of the $Cu_{64}Zr_{36}$ nanoparticles where the Cu and Zr atoms are colored red and blue, respectively. (b) Plan view of the stacked nanoparticles in the y-z plane with the atoms colored according to volumetric strain demonstrating the initial configuration is free of dilatations. (c) Atomic volume distribution of the nanoparticles relative to the BMG with a magnified view of the shoulder of the Cu peak shown in the inset.

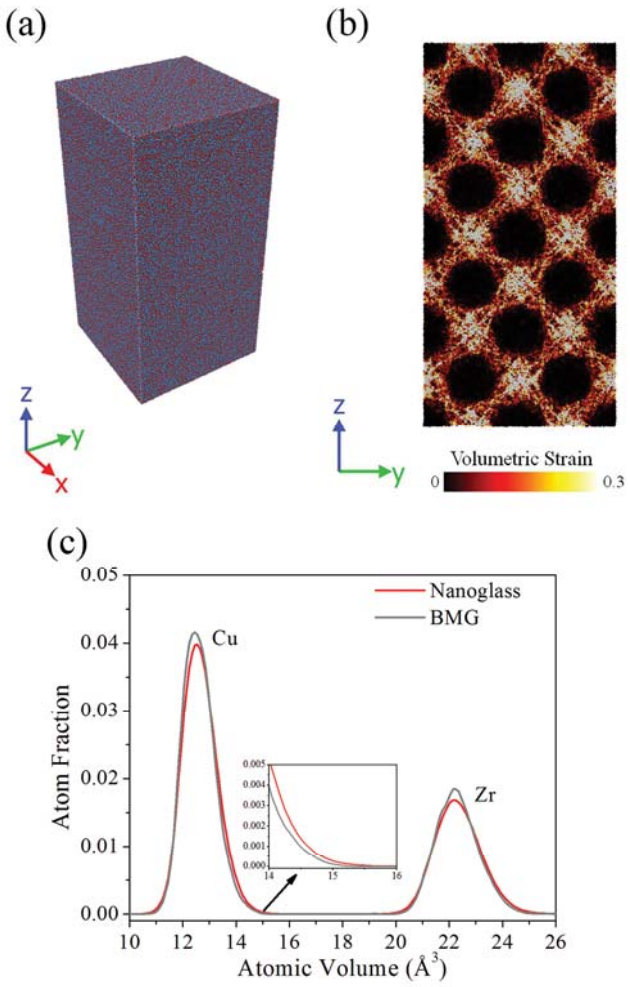

Fig. 2 (a) 3D representation of the consolidated nanoglass structure where the Cu and Zr atoms are colored red and blue, respectively. (b) Plan view with the atoms colored according to volumetric strain. (c) Atomic volume distribution of the consolidated nanoglass relative to the BMG with a magnified view of the shoulder of the Cu peak shown in the inset.

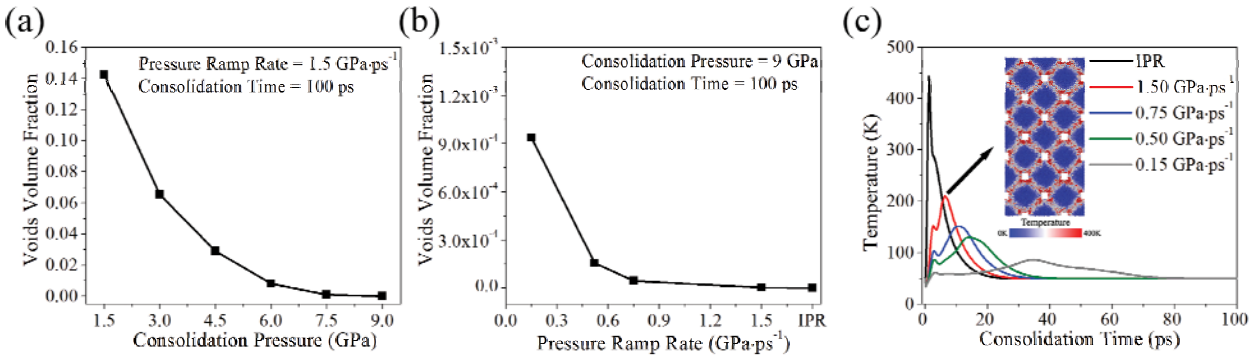

Fig. 3 Void volume fraction for the $Cu_{64}Zr_{36}$ nanoglass consolidated from 15 nm diameter nanoparticles as a function of (a) consolidation pressure and (b) pressure ramp rate where IPR represents the instantaneous pressure ramp condition. (c) Temperature profiles as a function of consolidation time for five different pressure ramp rates. A snapshot of the nanoglass consolidated at 1.50 GPa·ps^{-1} is shown at the peak temperature (t = 6.5 ps) in the inset with atoms colored according to instantaneous temperature and demonstrates that the temperature spikes derive primarily from the atoms within the surface layers of the nanoparticles during consolidation.

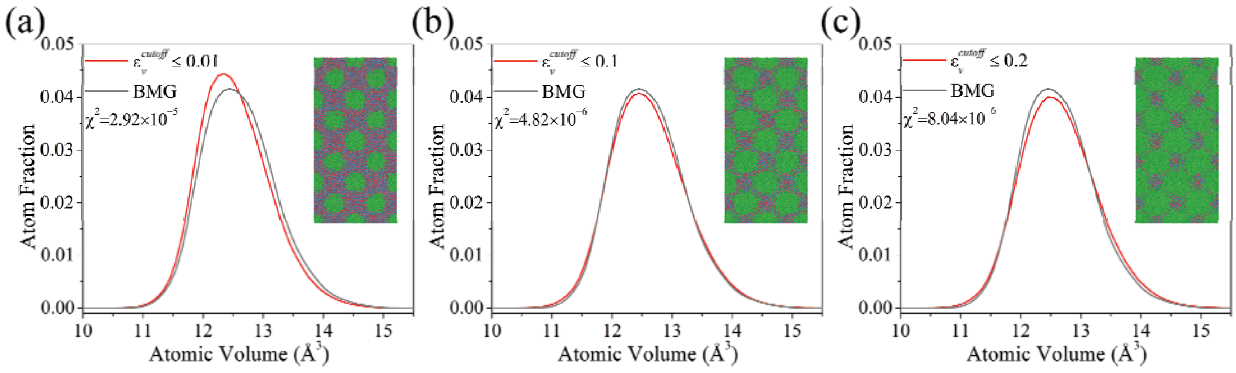

Fig. 4 Atomic volume distributions for a subset of atoms in the consolidated structure defined by volumetric strains of (a) $\boldsymbol{\varepsilon_v^{cutoff}} \leq 0.01$, (b) $\boldsymbol{\varepsilon_v^{cutoff}} \leq 0.1$, and (c) $\boldsymbol{\varepsilon_v^{cutoff}} \leq 0.2$. The atomic volume distribution of the BMG is shown for reference and only Cu peaks are depicted for clarify of presentation. The insets illustrate slices taken from the nanoglass along the y-z plane with atoms captured by the respective volumetric strain ranges (defined by $\boldsymbol{\varepsilon_v^{cutoff}}$) highlighted in green.

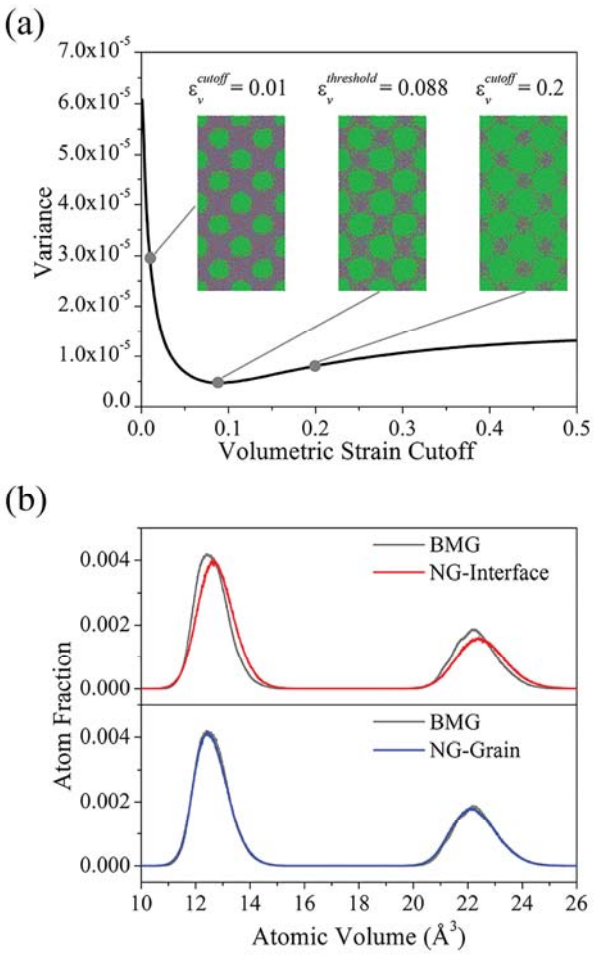

Fig. 5 (a) Variance as a function of the volumetric strain cutoff with insets illustrating slices taken from the nanoglass along the y-z plane with atoms captured by the respective volumetric strain ranges highlighted in green. (b) Atomic volume distributions for the atoms located in the interfaces (upper) and amorphous grains (lower) indexed based on the value of $\varepsilon_v^{threshold}$ identified from (a); the atomic volume distribution for the BMG is reproduced for reference.

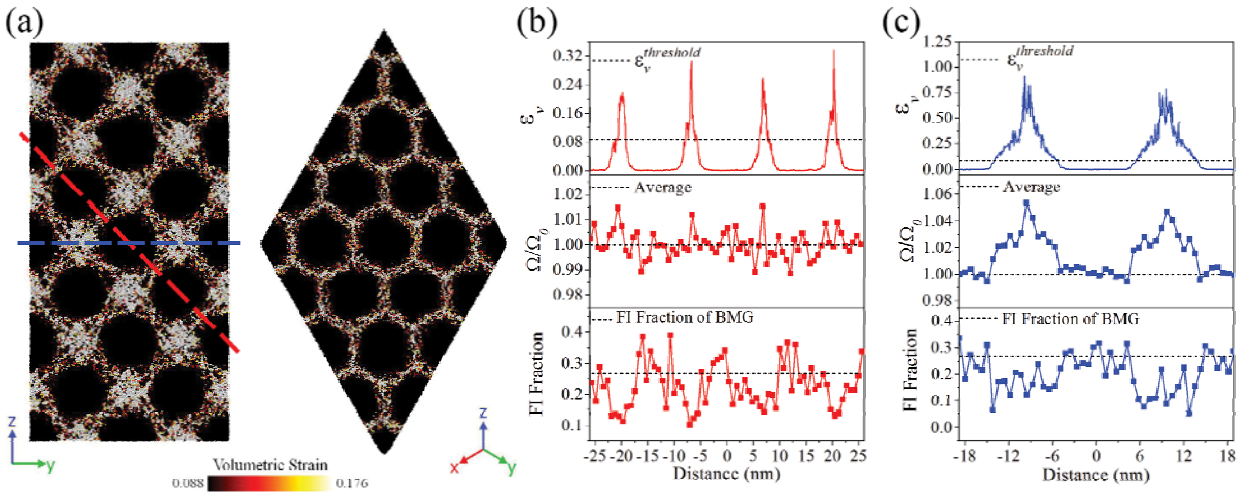

Fig. 6 (a) Two 5 nm thick slices extracted from the $Cu_{64}Zr_{36}$ nanoglass consolidated from 15 nm diameter nanoparticles along the y-z (left) and close-packed (right) planes with atoms colored by their value of volumetric strain. Volumetric strain (ε_v), atomic volume (Ω) normalized by the average atomic volume (Ω_0), and FI fraction mapped as a function of distance along the (b) red dashed line through the interfaces and (c) blue dashed line through the triple junctions. The reference zero point was assigned in the center of the amorphous grain at the intersection of the two dashed lines.

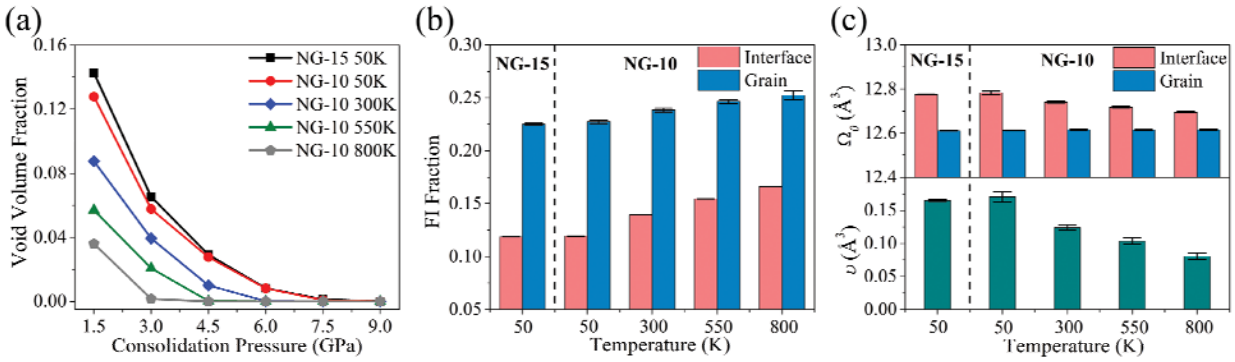

Fig. 7 (a) Void volume fraction as a function of consolidation pressure for the $Cu_{64}Zr_{36}$ nanoglass produced from 10 nm diameter nanoparticles using consolidation temperature of 50, 300, 550, and 800 K; the nanoglass produced from the 15 nm diameter nanoparticles is also shown for reference. (b) FI fraction delineated for the interfaces and amorphous grains as a function of consolidation temperature for both grain size nanoglasses separated by the vertical dashed line. (c) Average atomic volume (Ω_0) of the atoms within the interfacial region and amorphous grains and corresponding excess free volume (υ) for the different grain sizes and consolidation temperatures.

Graphical Abstract